Postoperative Impedance-Based Estimation of Cochlear Implant Electrode Insertion Depth

Stephan Schraivogel,[1,2] Philipp Aebischer,[1,2] Franca Wagner,[3] Stefan Weder,[2] Georgios Mantokoudis,[2] Marco Caversaccio,[1,2] and Wilhelm Wimmer[1,2,4]

Objectives: Reliable determination of cochlear implant electrode positions shows promise for clinical applications, including anatomy-based fitting of audio processors or monitoring of electrode migration during follow-up. Currently, electrode positioning is measured using radiography. The primary objective of this study is to extend and validate an impedance-based method for estimating electrode insertion depths, which could serve as a radiation-free and cost-effective alternative to radiography. The secondary objective is to evaluate the reliability of the estimation method in the postoperative follow-up over several months.

Design: The ground truth insertion depths were measured from postoperative computed tomography scans obtained from the records of 56 cases with an identical lateral wall electrode array. For each of these cases, impedance telemetry records were retrieved starting from the day of implantation up to a maximum observation period of 60 mo. Based on these recordings, the linear and angular electrode insertion depths were estimated using a phenomenological model. The estimates obtained were compared with the ground truth values to calculate the accuracy of the model.

Results: Analysis of the long-term recordings using a linear mixed-effects model showed that postoperative tissue resistances remained stable throughout the follow-up period, except for the two most basal electrodes, which increased significantly over time (electrode 11: ~10 Ω/year, electrode 12: ~30 Ω/year). Inferred phenomenological models from early and late impedance telemetry recordings were not different. The insertion depth of all electrodes was estimated with an absolute error of 0.9 mm ± 0.6 mm or 22° ± 18° angle (mean ± SD).

Conclusions: Insertion depth estimations of the model were reliable over time when comparing two postoperative computed tomography scans of the same ear. Our results confirm that the impedance-based position estimation method can be applied to postoperative impedance telemetry recordings. Future work needs to address extracochlear electrode detection to increase the performance of the method.

Key words: Anatomy-based fitting, Cochlear coverage, Electrode position, Follow-up, Hearing preservation, Radiation-free.

[1]Hearing Research Laboratory, ARTORG Center for Biomedical Engineering Research, University of Bern, Bern, Switzerland; [2]Department of Otorhinolaryngology, Head and Neck Surgery, Inselspital, Bern University Hospital, University of Bern, Bern, Switzerland; [3]Department of Diagnostic and Interventional Neuroradiology, Inselspital, Bern University Hospital, University of Bern, Bern, Switzerland; [4]Technical University of Munich, Germany; TUM School of Medicine, Klinikum rechts der Isar, Department of Otorhinolaryngology

INTRODUCTION

Cochlear implants (CIs) are highly effective neuroprostheses for patients with partial or complete deafness; it is estimated that more than 1 million systems have been implanted worldwide (Zeng 2022). In addition to restoring hearing through electrical stimulation of the auditory nerve, modern CIs have telemetry capabilities that enable the measurement of electrical impedances and neural responses. Impedance telemetry has been routinely used in clinical practice to check the integrity of the implant and to detect open or short circuits (Carlson et al. 2010). Furthermore, advances in impedance field telemetry (IFT) provide information about the patient's anatomy and CI electrode contacts (Vanpoucke et al. 2004; Tykocinski et al. 2005). This led several research groups to develop methods to infer electrode positions (de Rijk et al. 2020; Dong et al. 2021; Hou et al. 2021; Klabbers et al. 2021; Hoppe et al. 2022), the array orientation during insertion (Hafeez et al. 2021), and the proximity of contacts to the modiolus or the facial nerve (Giardina et al. 2017; Pile et al. 2017; Bruns et al. 2021; Sijgers et al. 2022) from IFT data.

In a previous study, a phenomenological model was proposed to estimate linear and angular insertion depths of CI arrays using intraoperative IFT recordings (Aebischer et al. 2020). The model is based on the correlation between a subcomponent of the measured clinical impedances and ground truth linear electrode insertion depth from computed tomography (CT) scans (obtained by manually labeling and calculating the linear distance of the electrodes from the round window [RW]). Since the definition of the cochlear view by Xu et al. (2000), knowledge of the CI insertion depth is of clinical importance for postoperative evaluation. Either immediately to verify the surgical outcome (O'Connell et al. 2016; Rathgeb et al. 2019) or later in the follow-up to monitor electrode migration (Dietz et al. 2016) or to explain parts of the variability in postoperative speech understanding outcomes (Chakravorti et al. 2019). In addition, CI audio processor fitting can be personalized to take into account patient anatomy and electrode locations, potentially improving hearing outcomes (Venail et al. 2015; Kurz et al. 2022; Mertens et al. 2022). The current gold standard for determining intracochlear electrode positions is radiography, which entails radiation exposure, requires dedicated infrastructure, and incurs additional costs, limiting its use in routine clinical practice (McCollough et al. 2015). Therefore, a cost-effective and radiation-free alternative method would be of great value to the clinical community, especially for children (Ehrmann-Müller

<zdoi; 10.1097/AUD.0000000000001379>

et al. 2020). Alternative methods could infer electrode positions using facial nerve stimulation (Herrmann et al. 2022), electrically evoked compound action potentials (Lambriks et al. 2023), or electrocochleography (O'Connell et al. 2017). In addition, the impedance-based estimation model proposed by Aebischer et al. (2020) showed potential applicability but was based on a small data set of intraoperative IFT recordings. Further analyses with larger sample sizes are needed to evaluate the method's applicability in the long term. This is especially important since clinical impedances are known to change during the postoperative follow-up period due to immune responses and intracochlear inflammatory reactions (Vargas et al. 2012; Wolf-Magele et al. 2015; Hu et al. 2020; Alhabib et al. 2021; Wimmer et al. 2022a).

Therefore, the aim of this study is to evaluate whether the method proposed by Aebischer et al. (2020) can also be applied to postoperative IFT recordings. We hypothesized that tissue resistances, subcomponents of clinical impedances, remain stable during postoperative follow-up, making the phenomenological model suitable for postoperative recordings.

MATERIALS AND METHODS

Study Design and Demographics

We performed a retrospective analysis of impedance telemetry and CT data from patients who underwent cochlear implantation between March 2015 and February 2021. The study was approved by our local institutional review board (ID 2019-01578). Only data from patients implanted with the electrode array most commonly used at our center (FLEX[28]; MED-EL, Austria) were included in the analysis.

Each patient was required to have a preoperative CT scan obtained during the assessment of eligibility for CI and at least one postoperative CT scan obtained either within 5 days of the implantation or within 5 days of the activation (day 28). In total, data were obtained for 56 cases from 48 patients (eight bilateral cases; 36 females and 20 males). The patients' age ranged from 0 to 81 years (median age 49 years), and there were 19 left and 37 right-sided implantations. In all cases, cochlear implantation was performed using a RW approach, and electrode arrays were stabilized with fat tissue and temporal fascia.

Impedance Telemetry Data

For each case, all available IFT recordings were retrieved from the day of implantation to the time of this study. All IFT data were recorded using the standard clinical protocol of the manufacturer's telemetry software (MAESTRO; MED-EL) with an amplitude and pulse width of approximately 300 μA and 27 μs, respectively. The voltage potential at the recording electrode was measured at the end of the second phase of the charge-balanced biphasic pulse (Zierhofer et al. 1997). IFT recordings were checked for anomalies such as short or open circuits detected by the telemetry software. If more than one electrode failed to record a valid potential (i.e., a short circuit or open circuit was detected), the respective IFT recording was excluded from the dataset. If the affected IFT was recorded closest to and thus associated with the first postoperative CT scan, the corresponding case was excluded from the study. Otherwise, data indicating a short circuit or open circuit in the recorded voltage matrix were interpolated from neighboring electrode contacts (in four IFT recordings from three cases). The voltage matrix was divided by the stimulation current to obtain the impedance matrix. Tissue resistances were calculated from the impedance matrix using bivariate spline extrapolation (Aebischer et al. 2020). Tissue resistances represent the electrical resistances of the biological tissue between the reference electrode on the implant body and the intracochlear electrode contacts (Vanpoucke et al. 2004).

Computed Tomography Data

Pre- and postoperative CT or cone beam CT scans were retrieved. The CT resolution for 56 cases with pre- and postoperative scans was between 0.15 mm and 0.43 mm, and the slice thickness was between 0.15 mm and 0.7 mm. A second postoperative CT scan was available for five bilateral cases after the first postoperative scan of the same ear.

Electrode Insertion Depth

The ground truth electrode insertion depths were extracted from CT scans and used as input data for the phenomenological model (Aebischer et al. 2020). For preoperative cochlear landmark and postoperative electrode contact labeling, the open-source software 3D Slicer (Fedorov et al. 2012) was used. The postoperative CT scans were co-registered to the preoperative CT scans using a rigid transform and mutual information metric (Klein et al. 2009) to reduce landmark labeling errors that could result from electrode
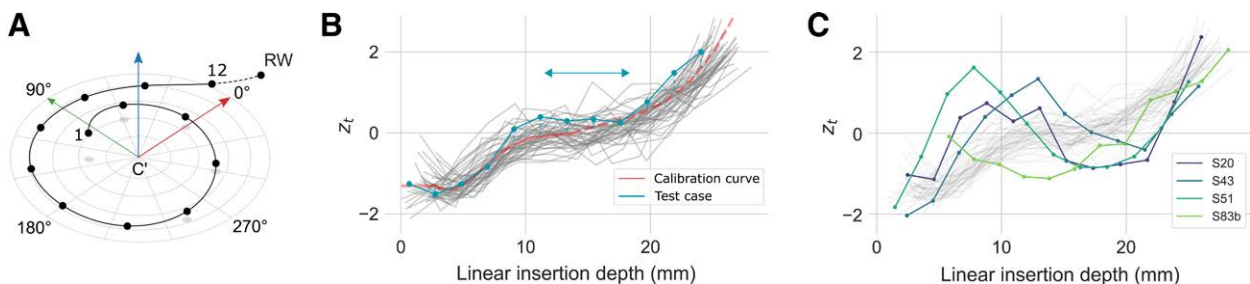

Fig. 1. A, Local coordinate system with the origin at the cochlear center C' for ground truth angular and linear electrode insertion depths (case 27b). The *x* axis, *y* axis, and *z* axis are indicated in red, green, and blue, respectively. The electrode contacts are numbered from apical to basal (1–12) and connected by a spline approximation, depicted as a solid black curve. The dashed line starting at the RW landmark represents the (positive) linear insertion depth of the most basal electrode 12. B, Standardized tissue resistances z_t vs. ground truth linear electrode insertion depth of all cases with a fully inserted electrode array (N = 46). As an example, the calibration curve for case 12a (i.e., from all cases except case 12a) is shown in red. The basal and apical fit of the calibration curve are depicted by the solid and dashed red line, respectively. A test case's telemetry recording and the minimization along the *x* axis are depicted in blue. C, The same calibration data as in (B) are shown, but 4 additional cases are highlighted, which exhibit large deviations from the calibration data due to otosclerosis (case 20 and 43), enlarged vestibular aqueduct (case 51), and Ménière's disease (case 83b).

array artifacts (Benson et al. 2022). Subsequently, we measured the cochlear base length and width (Rathgeb et al. 2019) and labeled the electrodes using maximum intensity projection. A local coordinate system (Fig. 1A) was formed (Verbist et al. 2010), where a robust cochlear modiolar axis detection algorithm defined the z axis (Wimmer et al. 2019). The x axis passed through the landmarks C' (origin) and RW, where C' is the orthogonal projection of RW onto the z axis (Wimmer et al. 2014). With the y axis passing through C', an orthonormal basis was formed. The ground truth linear insertion depth was computed by numerically integrating a quadratic spline fit through the RW landmark and all electrodes (Fig. 1A). An electrode was labeled with a negative linear insertion depth (i.e., the electrode position was extracochlear) if its x coordinate was greater than the x coordinate of the RW landmark. In 47 cases, the electrode arrays were fully inserted into the cochlea. Partially inserted electrode arrays were present in nine cases (three cases each with one, two, and three extracochlear electrodes, respectively; see demographics Table S1 in Supplemental Digital Content 2, http://links.lww.com/EANDH/B142).

Tissue Resistances

Over time, electrode impedances can change due to inflammatory processes and the formation of intracochlear tissue (Rahman et al. 2022; Wimmer et al. 2022a). Since tissue resistances were used as input data for the phenomenological model, we analyzed their stability over time. To evaluate the long-term stability of tissue resistances, we included data covering a minimum of 12 mo up to a maximum postoperative follow-up of 60 mo, resulting in analyses of 42 cases with full array insertions. A linear mixed-effects model with case-level random intercepts and random slopes was used to assess the long-term stability of tissue resistances (in kΩ). For the model, the postoperative follow-up (in months) was used as the independent variable. In addition, the side of the implantation (left versus right), age (in years), gender (male versus female), and an interaction term between postoperative follow-up time and electrode number (categorical, 1 to 12) were included as fixed effects. A p-value of less than 0.05 was considered as statistically significant. The statistical analysis was performed in the RStudio environment (RStudio Team, 2022), using the lme4 package (Bates et al. 2015).

Insertion Depth Estimation Model

The linear insertion depth was estimated with a phenomenological model adapted from Aebischer et al. (2020). Tissue resistances were computed using bivariate spline extrapolation of the IFT recordings. Each test case refers to an implanted side of a patient whose insertion depth was estimated using the model. Before curve fitting, the tissue resistances were standardized to z-scores by subtracting the mean and dividing by the SD of the tissue resistances of the corresponding case. The standardized tissue resistances z_t are unitless, centered on a mean value of zero, and normalized to unit variance.

The linear electrode insertion depth of a test case was found through the minimization of an objective function defined as the sum of squared residuals between the standardized tissue resistances and a calibration curve derived from calibration data (Aebischer et al. 2020), which is depicted in Figure 1B. The calibration curve was composed of two separate parts, with the median linear insertion depth of the calibration data dividing it into a basal and an apical fit (Fig. 1B). The basal fit (solid line) was realized as a

one-dimensional spline with five explicit knots based on the entire calibration data. The basal fit was constrained to the fifth to 95th percentiles of the calibration data. Outside the fitting interval, i.e., beyond the most basal electrode, a constant extrapolation was chosen to stay within a physiologically reasonable range of standardized tissue resistances. The apical fit (dashed line) was realized as a third-degree polynomial based on the upper half of sorted calibration data (starting with the median). Standardized tissue resistances z_t were checked for outliers per electrode. Based on the median absolute deviation, four cases with full insertions were excluded from further analysis (see Fig. S6 in Supplemental Digital Content 1, http://links.lww.com/EANDH/B141, which shows the outlier detection method). The resulting calibration curve of the model and the excluded cases are shown in Figures 1B, C. The estimated linear insertion depth was converted to angular values based on a previously established method, taking into account the cochlear base length (Anschuetz et al. 2018; Aebischer et al. 2020).

Comparison of Early and Late Models

For the calibration data used in this study, IFT recordings and CT scans were divided into two categories based on their acquisition date. Early calibration data consisted of IFT and CT data acquired within 5 days of the implantation (days 0 to 5). Late calibration data were acquired within 5 days of the activation (days 28 to 33; see Table S1 in Supplemental Digital Content 2, http://links.lww.com/EANDH/B142). To enlarge the resulting calibration data by merging early and late data, we evaluated whether there was a difference between early and late phenomenological models. For this purpose, a linear mixed-effects model with case-level random intercepts was used. The ground truth linear insertion depth (in mm) and the calibration category (early versus late) were used as the independent variables.

Performance of Insertion Depth Estimation

Because the statistical analysis of standardized tissue resistances revealed no difference between early and late calibration data, as discussed below, a single calibration curve was constructed from the merged data. The merged calibration data consisted of the standardized tissue resistances and ground truth linear insertion depths of all cases in the dataset, but with the test case excluded. The calibration curve was then used to estimate the electrode insertion depth of the test case and compare it with the ground truth electrode positions from the corresponding CT scan.

The analysis was split into two parts to account for cases with electrodes fully inserted into the cochlea and cases with at least one extracochlear electrode. First, the performance was analyzed using only data from fully inserted electrode arrays (N = 47) in a leave-one-out cross-validation. Since the phenomenological model required separate calibration and test data, this resulted in a different calibration curve for each test case. Second, the calibration data consisted of the same cases with fully inserted electrode arrays as in the first analysis but applied to cases with at least one extracochlear electrode (N = 9). The mean and SD of the linear and angular absolute errors were calculated to assess the accuracy and precision of the insertion depth estimation. The absolute error was calculated as the difference between the ground truth values from CT scans and insertion depth values estimated by the phenomenological model.
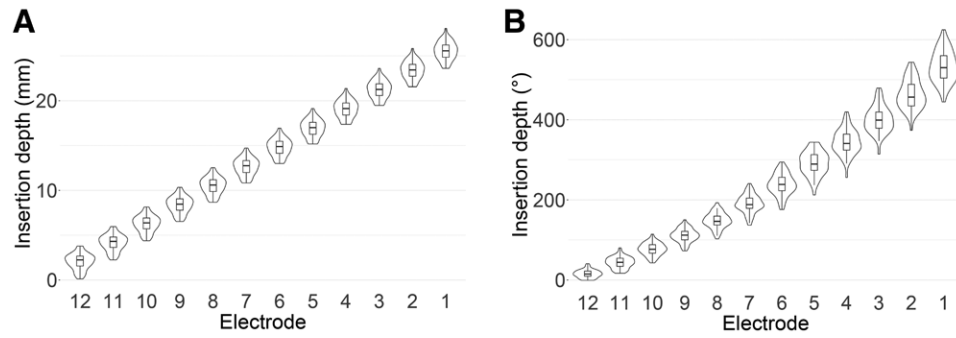
Fig. 2. Distributions of ground truth (A) linear and (B) angular insertion depth for 47 cases with a fully inserted electrode array. Electrodes are numbered from apical to basal (1–12).

Long-Term Stability of the Phenomenological Model

In our data set, five patients with bilateral implants underwent another postoperative CT scan after cochlear implantation of the second ear, on which the first CI was visible. To minimize errors caused by misalignment of the image data, the first and second postoperative CT scans were co-registered to the same preoperative CT scan. To assess the long-term stability of the phenomenological model, the electrode insertion depth was estimated from IFT data at two different time points, recorded closest to the first and second CT scans, respectively. Subsequently, the absolute estimation error was compared at both time points for all patients. The calibration data set consisted of the same cases with fully inserted electrode arrays as in the analysis of model performance (N = 47).

RESULTS

Ground Truth Electrode Positions

Figure 2 summarizes the ground truth linear and angular electrode insertion depths of all cases with a fully inserted electrode array (N = 47). We measured a minimum insertion depth of the most basal electrode of −5.9 mm and a maximum of 3.8 mm. The mean basal electrode insertion depth of all fully inserted arrays was 2.1 mm. For cases with extracochlear electrodes, the

mean insertion depth of the most basal electrode was −1.3 mm, −3.6 mm, and −5 mm for one, two, and three extracochlear electrodes, respectively.

Long-Term Stability of Tissue Resistances

A total of 485 IFT recordings from the 42 cases were included in the model. An average tissue resistance of 1.5 kΩ for the most apical electrode was found (95% confidence interval, 1.4 to 1.6 kΩ; see Table S2 in Supplemental Digital Content 2, http://links.lww.com/EANDH/B142). The electrode number had a statistically significant negative effect on tissue resistance, which increased from the second-most apical electrode to the most basal electrode (with a difference of −0.5 to −0.1 kΩ compared to the tissue resistance of the most apical electrode; $p < 0.001$ for all electrodes). This was expected because more basally located electrodes should be associated with lower tissue resistances due to the larger perilymph volume and resulting higher electrical conductivity in the scala tympani (Aebischer et al. 2020). The postoperative follow-up time had a significant effect on tissue resistance (with an average increase of 34 Ω per year at all electrodes across all cases; $p < 0.001$). Male patients had significantly lower tissue resistances than females (−141 Ω; $p = 0.005$). No significant effects of side or age were found. Further,
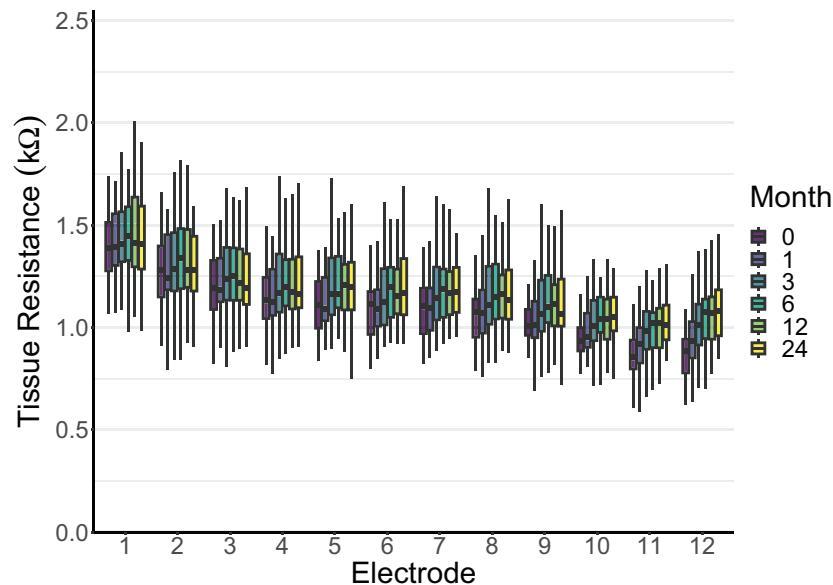

Fig. 3. Tissue resistances of 32 fully inserted cases. Results are shown for all electrodes at the intraoperative measurement (month 0), first activation session (month 1), and follow-up fitting sessions (months 3–24). Electrodes are numbered from apical to basal (1–12).

Fig. 4. Standardized tissue resistances z_t of 32 fully inserted cases. Results are shown for all electrodes at the intraoperative measurement (month 0), first activation session (month 1), and follow-up fitting sessions (months 3–24). Electrodes are numbered from apical to basal (1–12).
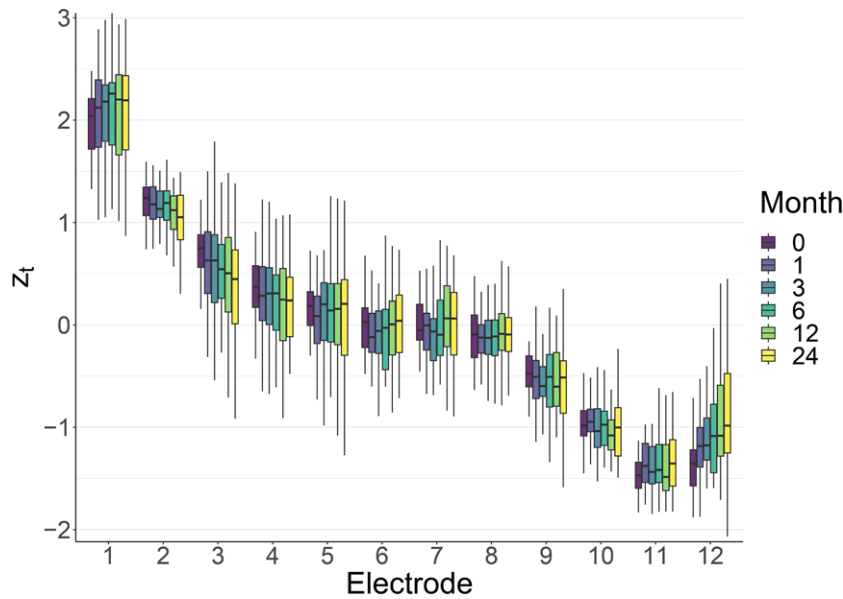
a statistically significant interaction between postoperative follow-up time and electrode number was observed for the 2 most basal electrodes (12 Ω per year; $p = 0.02$ and 28 Ω per year; $p < 0.001$ for the second to the most basal electrode, respectively). This indicates that tissue resistances generally remained stable for all but the two most basal electrodes. Figure 3 summarizes the time course of tissue resistance for 32 cases for which a complete set of IFT recordings (i.e., for the intraoperative session and follow-up at 1, 3, 6, 12, and 24 mo) was available. In general, tissue resistances were lowest for the intraoperative IFT recordings. Consistent with the statistics (Table S2 in Supplemental Digital Content 2, http://links.lww.com/EANDH/B142), tissue resistances mostly increased slightly over the follow-up period, with the largest increase at electrodes 11 and 12. Figure 4 shows the same data presented as standardized tissue resistances z_t, which served as input for the estimation model. Here, electrode 12 shows the largest increase over time.

Comparison of Early and Late Models

The distribution of CT scan acquisition days since implantation for all cases is summarized in Figure S4 in Supplemental Digital Content 1, http://links.lww.com/EANDH/B141. Most postoperative CT scans were acquired on the day of implantation or the day of the first activation session (28 days thereafter). No statistically significant differences between the early and late phenomenological models were found ($p = 0.15$; see Fig. 5 and Table S3 in Supplemental Digital Content 2, http://links.lww.com/EANDH/B142).

Performance of Insertion Depth Estimation

Figure 6 shows the insertion depth estimation errors based on first CT scans and corresponding IFT recordings for all 47 cases with fully inserted electrode arrays in the merged model. The linear insertion depth error of the impedance-based estimation ranged between −1.6 mm and 3.2 mm, resulting in an
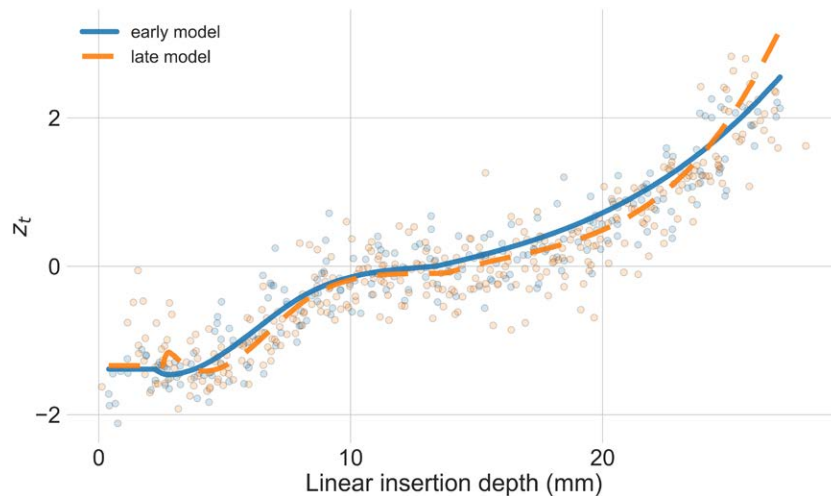

Fig. 5. Standardized tissue resistances z_t vs. ground truth linear insertion depth of 47 cases with a fully inserted electrode array. The category for subdividing the calibration data is color coded (early category in blue with N = 19 cases and late category in orange with N = 28 cases). The calibration data is depicted by a scatter plot. The resulting calibration curve for both categories is depicted by a solid and dashed line, respectively.
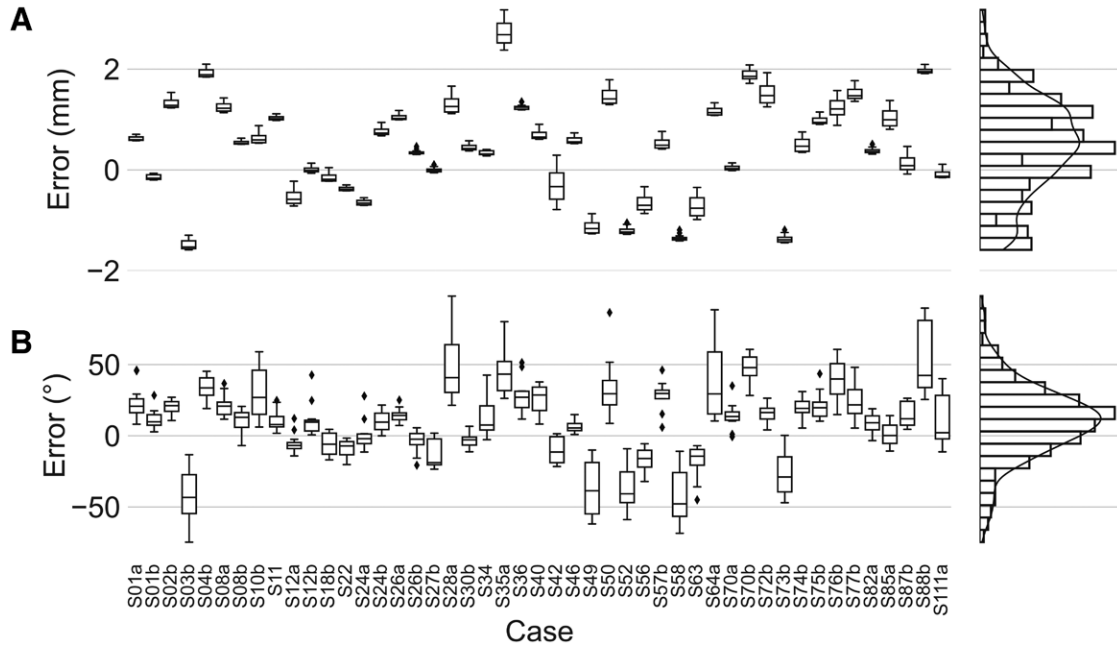
Fig. 6. Box plot with a histogram of the early and late insertion depth estimation errors of 47 cases with a fully inserted electrode array. A, Linear insertion depth estimation error. B, Angular insertion depth estimation error.

absolute error of $0.88\,mm \pm 0.6\,mm$ (mean ± SD). Expressed as angular insertion depth, the estimation error was between −75° and 98° angle, corresponding to an absolute error of 22° ± 18° angle. A systematic underestimation was found for both error distributions (mean error of 0.4 mm and 10° angle, respectively). The distribution of the absolute linear and angular estimation errors is depicted in Figure S2 in Supplemental Digital Content 1, http://links.lww.com/EANDH/B141. In cases with partial insertions, the mean absolute estimation error increased to 2.7 mm, 4.6 mm, and 5.2 mm for one, two, and three extracochlear electrodes, respectively.

Long-Term Stability of the Phenomenological Model

Figure 7 compares the IFT recordings of one case closest to the first and second CT scans. Consistent with Figure 4, standardized tissue resistances were stable at all electrodes except the most basal electrode. For all cases with a second CT scan

and a corresponding IFT recording within 50 days (N = 5), the mean absolute error of estimated electrode insertion depth was comparable for the first and the second CT scan. The merged model estimated electrode insertion depth with an absolute error of $0.6\,mm \pm 0.3\,mm$ and $0.4\,mm \pm 0.3\,mm$ (mean ± SD) compared to the first and second CT scans, respectively (see Table S4 in Supplemental Digital Content 2, http://links.lww.com/EANDH/B142).

DISCUSSION

In this study, we demonstrated that the phenomenological model can estimate intracochlear electrode positions in intraoperative and postoperative settings because the respective phenomenological models did not differ. Using the merged calibration data, we were able to evaluate the performance and long-term stability of the phenomenological model with two postoperative CT scans.
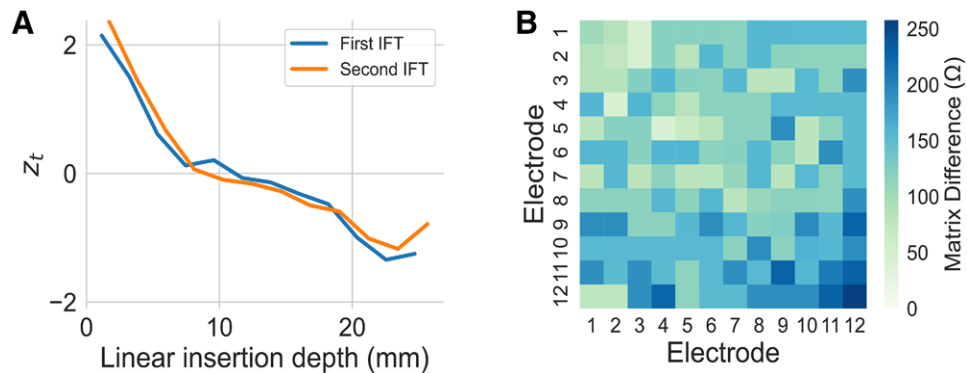

Fig. 7. Illustration of a case (24a) with 2 postoperative CT scans and corresponding IFT separated by 20 mos. A, Comparison of standardized tissue resistances z_t and (B) difference between impedance matrices (second minus first measurement) with tissue resistances on the diagonal from the 2 IFT recordings. Electrodes are numbered from apical to basal (1–12).

Performance and Long-Term Stability of the Phenomenological Model

The estimation accuracy from early and late IFT recordings for the 47 fully inserted cases was comparable to that reported in Aebischer et al. (2020). Our extended analysis confirmed that the phenomenological model can achieve an accuracy of, on average, less than 1 mm. This corresponds to about half the electrode spacing (i.e., half of 2.1 mm for FLEX[28] arrays). However, this was not true for cases with partially inserted electrode arrays, which, when included, resulted in lower estimation accuracy and precision. Therefore, a robust method for detecting extracochlear electrodes is needed to increase the accuracy of the insertion depth estimate. Based on ground truth values from the first postoperative CT scans, the comparison of early and late model performance showed that the estimation accuracy of the late model was better than that of the early model in a leave-one-out cross-validation (see diagonal of Fig. S5 in Supplemental Digital Content 1, http://links.lww.com/EANDH/B141). The early model is based on only a few cases (N = 19 compared to N = 28 cases in the late model), which may explain the difference in performance. The performance of the estimates using the late model for early data and vice versa was comparable. In five bilateral cases with a second postoperative CT scan, a comparable performance of the early, late, and merged models was observed over time (see Table S4 in Supplemental Digital Content 2, http://links.lww.com/EANDH/B142). Encouragingly, the performance of the phenomenological model remained stable over time despite the increase in tissue resistance at the basal electrodes. This extends the potential use of the phenomenological model to postoperative applications.

Long-Term Stability of Tissue Resistances

Ongoing research aims to determine whether CI impedances can be biomarkers of traumatic intracochlear events and inflammatory responses (Shaul et al. 2019; Ausili et al. 2022; Leblans et al. 2022; Wimmer et al. 2022a). The basal turn of the cochlea is reported to be more exposed to severe intracochlear trauma and tissue reactions (Seyyedi & Nadol Jr. 2014; Aebischer et al. 2021; Rahman et al. 2022). Reported stabilization times of impedances after cochlear implantation range from 3 to 8 wks (Hu et al. 2020; Parreño et al. 2020) up to 6 mo for the most basal electrodes (Molisz et al. 2015). A small but significant positive effect of time on tissue resistances was found (see Table S2 in Supplemental Digital Content 2, http://links.lww.com/EANDH/B142). This increase was indeed most pronounced at the basal electrodes (Fig. 3). The time-associated effects of tissue resistances could result from short-term foreign body reactions, inflammation, or wound healing (Parreño et al. 2020). Correspondingly, the median clinical impedances increased monotonically only for the two most basal electrodes (see Fig. S1 in Supplemental Digital Content 1, http://links.lww.com/EANDH/B141).

As previously described by Wimmer et al. (2022a), a U-shaped distribution was observed with higher clinical impedances at the apical and basal electrodes and lower clinical impedances at the middle electrodes. This U-shaped distribution is not seen in the progression of tissue resistances, which remained comparatively stable over the postoperative follow-up. Near-field and far-field resistances in an equivalent circuit model describe separate contributions to the overall clinical impedance measured at the stimulating electrode (Vanpoucke et al. 2004). Tissue resistance corresponds to the far-field resistance, i.e., the resistance to electric current through biological tissue from the stimulating electrode to the ground electrode (Aebischer et al. 2020). In contrast, the clinical impedance includes the near-field resistance, which is thought to provide information about the cochlear micro-environment near the stimulating electrode and could be associated with residual hearing outcomes (Wimmer et al. 2022a). Tissue resistances of male patients were significantly lower than those of female patients (see Table S2 in Supplemental Digital Content 2, http://links.lww.com/EANDH/B142 and Fig. S3 in Supplemental Digital Content 1, http://links.lww.com/EANDH/B141). Since the shape of the cochlea is sex-dependent (Braga et al. 2019), one explanation for the difference in tissue resistance could be that the cochleae of males are significantly longer than those of females (33.1 mm for females versus 34.7 mm for males, $p < 0.001$; two-sample, two-sided t test). This could be associated with a larger available intracochlear volume and therefore less resistance (Baguant et al. 2022). However, this finding did not affect the phenomenological model because tissue resistances were standardized. Standardized tissue resistances showed no significant difference between female and male patients.

Detection of Pathological Cochlear Conditions

The calibration curve of cases with normal anatomy can be characterized in three sections (Fig. 1B). In the basal section, the calibration curve approximately follows a logistic function, reaching a plateau in the middle section. In the apical section, the curve approximately follows an exponentially increasing function. Our data contained four cases with a remarkably different curve morphology of tissue resistance compared to the regular cases (Fig. 1C and Fig. S6 in Supplemental Digital Content 1, http://links.lww.com/EANDH/B141). These cases were associated with otosclerosis (cases 20 and 43), an enlarged vestibular aqueduct condition (case 51), and Ménière's disease (case 83b).

Otosclerosis causes abnormal bone remodeling in the middle ear, primarily affecting the RW, oval window, and structures adjacent to the cochlea (Frisch et al. 2000). The condition can lead to sensorineural hearing loss and, in patients with far-advanced otosclerosis, to facial nerve stimulation and electrode dislocation (Dumas et al. 2018). Another reported symptom of otosclerosis is partial obstruction of the scala tympani (Lee et al. 2011). Since these pathological features directly affect tissue conductivity and thus the basis of the estimation model, they may bias its result. For case 20, this would explain the deviation from the calibration curve at electrodes 8 to 10 (Fig. 1C) in the basal turn (corresponding to an insertion depth of 10.3 mm and 6.1 mm for electrodes 8 and 10, respectively). For case 43, the deviation from the calibration curve was mainly observed at electrodes 7 (12.3 mm) and 8 (10.2 mm).

Case 51 was diagnosed with an enlarged vestibular aqueduct, which is often associated with sensorineural hearing loss (Wimmer et al. 2022b) and an alteration in the ionic composition of perilymph and endolymph. This affects the propagation of the stimulation current in the cochlea, resulting in abnormally high intraoperative impedance values (Li et al. 2022). Figure 1C shows this effect as observed in case 51 at electrodes 8 (9.3 mm) to 11 (2.9 mm).

Ménière's disease is associated with fluctuating sensorineural hearing loss, aural fullness, spontaneous attacks of vertigo, and tinnitus (Minor et al. 2004). The condition can lead to impedance changes (McNeill & Eykamp, 2016), which could be related to the reduction of intracochlear volume due to endolymphatic hydrops (Fukushima et al. 2022). For case 83b, this would explain the deviation from the calibration curve at electrodes 7 (15.2 mm) to 10 (9.2 mm).

Study Limitations and Outlook

Our calibration data could include errors related to the resolution of clinical CT imaging. The average imaging resolution in the 56 cases was 0.18 mm and 0.21 mm (x and y axes) and 0.29 mm and 0.26 mm (z axis) for the preoperative and postoperative CT scans, respectively. Inaccurate preoperative cochlear landmark and postoperative electrode contact labeling are possible due to the limited CT resolution.

Moreover, the quantization of the voltage matrix can limit accuracy. Also taking into account the noise floor from CT scans and interelectrode spacing (SDs of around 0.04 mm), we calculated a total noise floor of approximately 0.4 mm ± 0.3 mm (mean ± SD). Compared with the absolute estimation error reported in this study (0.9 mm ± 0.6 mm from 47 cases), the absolute estimation error is already in the same order of magnitude as the noise floor. New IFT paradigms could improve the accuracy by measuring with higher resolution or providing measurements of impedance subcomponents (Aebischer et al. 2020; Di Lella et al. 2020). A limitation of the current phenomenological model is that it is susceptible to inaccuracies in the presence of extracochlear electrodes. Therefore, improved extracochlear electrode detection and confidence measures will be required to enable reliable interpretation of IFT data from partial insertions.

The phenomenological model was evaluated with only one type of electrode array, and future work will need to assess its applicability to other types.

The stability of the phenomenological model was assessed in only five cases for which a second postoperative CT scan was available. Future studies are needed to verify our results in more such cases. In addition, electrode migration may occur between the IFT recording and the corresponding CT scan, which could distort the data, ultimately reducing the accuracy and precision of the phenomenological model. However, the maximum time interval between IFT recordings and CT scans of the calibration data was only 1 day. The FLEX[28] array covers a distance of 23.1 mm between the first and last electrode, resulting in an interelectrode spacing of 2.1 mm. Ground truth deviations from the expected interelectrode spacing may be due to labeling inaccuracies resulting from the limited resolution of CT scans, manufacturing tolerances, and electrode array bending. A custom labeling pipeline in 3DSlicer was used, while other image analysis software such as Amira (FEI, Burlington, MA, USA) or OTOPLAN (Gerber et al. 2014) could be used alternatively.

CONCLUSIONS

We evaluated the applicability of a radiation-free impedance-based CI electrode position estimation method during and after CI insertion. We demonstrated that the phenomenological models from early and late IFT recordings did not differ. Therefore, the phenomenological model is also applicable for postoperative IFT data to estimate CI electrode insertion depth. In a test with 47 cases of fully inserted arrays, the model provided an accurate estimation of electrode insertion depth with an absolute error of 0.9 mm ± 0.6 mm (mean ± SD).

However, better sensitivity for extracochlear electrodes is required to provide reliable estimations for partial insertions as well. The proposed method could enable clinical applications, including intraoperative assessment of electrode locations, monitoring of postoperative electrode migration, or anatomy-based fitting without exposing patients to additional radiation.

Address for correspondence: Wilhelm Wimmer, Hearing Research Laboratory, ARTORG Center, University of Bern, Murtenstrasse 50, 3008 Bern, Switzerland. E-mail: wilhelm.wimmer@unibe.ch

REFERENCES

Aebischer, P., Meyer, S., Caversaccio, M., Wimmer, W. (2020). Intraoperative impedance-based estimation of cochlear implant electrode array insertion depth. *IEEE Trans Biomed Eng*, 68, 545–555.

Aebischer, P., Mantokoudis, G., Weder, S., Anschuetz, L., Caversaccio, M., Wimmer, W. (2021). In-vitro study of speed and alignment angle in cochlear implant electrode array insertions. *IEEE Trans Biomed Eng*, 69, 129–137.

Alhabib, S. F., Abdelsamad, Y., Yousef, M., Alzhrani, F., Hagr, A. (2021). Effect of early activation of cochlear implant on electrode impedance in pediatric population. *Int J Pediatr Otorhinolaryngol*, 140, 110543.

Anschuetz, L., Weder, S., Mantokoudis, G., Kompis, M., Caversaccio, M., Wimmer, W. (2018). Cochlear implant insertion depth prediction: A temporal bone accuracy study. *Otol Neurotol*, 39, e996–e1001.

Ausili, S. A., Parreño, M., Fernandez, F., Boccio, C. M., Di Lella, F. A. (2022). Biological response dynamics to cochlear implantation: Modeling and modulating the electrode-tissue interface. *Ear Hear, 43,* 1687–1697.

Baguant, A., Cole, A., Vilotitch, A., Quatre, R., Schmerber, S. (2022). Difference in cochlear length between male and female patients. *Cochlear Implants Int, 23,* 326–331.

Bates, D., Mächler, M., Bolker, B., Walker, S. (2015). Fitting linear mixed-effects models using lme4. *Journal of Statistical Software*, 67, 1–48.

Benson, J. C., Nassiri, A. M., Saoji, A. A., Carlson, M. L., Lane, J. I. (2022). Co-registration of pre-and post-operative images after cochlear implantation: A proposed technique to improve cochlear visualization and localization of cochlear electrodes. *Neuroradiol J, 36,* 194–197.

Braga, J., Samir, C., Risser, L., Dumoncel, J., Descouens, D., Thackeray, J. F., Balaresque, P., Oettlé, A., Loubes, J. -M., Fradi, A. (2019). Cochlear shape reveals that the human organ of hearing is sex-typed from birth. *Sci Rep, 9,* 10889.

Bruns, T., Riojas, K., Labadie, R. F., Webster, R. J. (2021). Real-time localization of cochlear-implant electrode arrays using bipolar impedance sensing. *IEEE Trans Biomed Eng, 69,* 718−724.

Carlson, M. L., Archibald, D. J., Dabade, T. S., Gifford, R. H., Neff, B. A., Beatty, C. W., Barrs, D. M., Driscoll, C. L. (2010). Prevalence and timing

of individual cochlear implant electrode failures. *Otol Neurotol*, *31*, 893–898.

Chakravorti, S., Noble, J. H., Gifford, R. H., Dawant, B. M., O'Connell, B., Wang, J., Labadie, R. F. (2019). Further evidence of the relationship between cochlear implant electrode positioning and hearing outcomes. *Otol Neurotol*, *40*, 617.

Dietz, A., Wennström, M., Lehtimäki, A., Löppönen, H., Valtonen, H. (2016). Electrode migration after cochlear implant surgery: More common than expected? *Eur Arch Otorhinolaryngol*, *273*, 1411–1418.

Di Lella, F. A., Parreño, M., Fernandez, F., Boccio, C. M., Ausili, S. A. (2020). Measuring the electrical status of the bionic ear. re-thinking the impedance in cochlear implants. *Front Bioeng Biotechnol*, *8*, 568690.

Dong, Y., Briaire, J. J., Siebrecht, M., Stronks, H. C., Frijns, J. H. (2021). Detection of translocation of cochlear implant electrode arrays by intra-cochlear impedance measurements. *Ear and Hearing*, *42*, 1397.

Dumas, A. R., Schwalje, A., Franco-Vidal, V., Bebear, J., Darrouzet, V., & Bonnard, D. (2018). Cochlear implantati on in far-advanced otosclerosis: Hearing results and complications. *Acta Otorhinolaryngol Ital*, *38*, 445.

Ehrmann-Müller, D., Shehata-Dieler, W., Kaulitz, S., Back, D., Kurz, A., Ku¨hn, H., Hagen, R., Rak, K. (2020). Cochlear implantation in children without preoperative computed tomography diagnostics. analysis of procedure and rate of complications. *Int J Pediatr Otorhinolaryngol*, *138*, 110266.

Fedorov, A., Beichel, R., Kalpathy-Cramer, J., Finet, J., Fillion-Robin, J. -C., Pujol, S., Bauer, C., Jennings, D., Fennessy, F., Sonka, M., Buatti, J., Aylward, S., Miller, J. V., Pieper, S., Kikinis, R. (2012). 3d slicer as an image computing platform for the quantitative imaging network. *Magn Reson Imaging*, *30*, 1323–1341.

Frisch, T., Sørensen, M. S., Overgaard, S., Bretlau, P. (2000). Predilection of otosclerotic foci related to the bone turnover in the otic capsule. *Acta Otolaryngol*, *120*, 111–113.

Fukushima, M., Akahani, S., Okamoto, H., Takeda, N., Inohara, H. (2022). Assessment of inner ear morphology and function in response to local positive pressure for ménière's disease: A nonrandomized controlled trial. *Sci Rep*, *12*, 20782.

Gerber, N., Bell, B., Gavaghan, K., Weisstanner, C., Caversaccio, M., Weber, S. (2014). Surgical planning tool for robotically assisted hearing aid implantation. *Int J Comput Assist Radiol Surg*, *9*, 11–20.

Giardina, C. K., Krause, E. S., Koka, K., Fitzpatrick, D. C. (2017). Impedance measures during in vitro cochlear implantation predict array positioning. *IEEE Trans Biomed Eng*, *65*, 327–335.

Hafeez, N., Du, X., Boulgouris, N., Begg, P., Irving, R., Coulson, C., Tourrel, G. (2021). Electrical impedance guides electrode array in cochlear implantation using machine learning and robotic feeder. *Hear Res*, *412*, 108371.

Herrmann, D. P., Müller-Graff, F. -T., Kaulitz, S., Cebulla, M., Kurz, A., Hagen, R., Neun, T., Rak, K. (2022). Application of intentional facial nerve stimulation during cochlear implantation as an electrophysiological tool to estimate the intracochlear electrode position. *Sci Rep*, *12*, 13426.

Hoppe, U., Brademann, G., Stöver, T., de Miguel, A. R., Cowan, R., Manrique, M., Falcón-González, J. C., Hey, M., Baumann, U., Huarte, A., Liebscher, T., Bennett, C., English, R., Neben, N., Macías, A. R. (2022). Evaluation of a transimpedance matrix algorithm to detect anomalous cochlear implant electrode position. *Audiol Neurootol*, *27*, 347–355.

Hou, L., Du, X., Boulgouris, N. V., Hafeez, N., Coulson, C., Irving, R., Begg, P., Brett, P. (2021). A capacitive cochlear implant electrode array sensing system to discriminate fold-over pattern. *J Speech Lang Hear Res*, *64*, 3685–3696.

Hu, H. -C., Chen, J. K. -C., Li, L. P. -H., Chen, W. K. -H., Huang, M. -J., Yeh, C. -H., Chen, L. -C., & Tung, T. -H. (2020). Evolution of impedance values in two different electrode array designs following activation of cochlear implants 1 day after surgery: A study of 58 patients. *Clin Otolaryngol*, *45*, 584–590.

Klabbers, T. M., Huinck, W. J., Mylanus, E. A. (2021). Comparison between transimpedance matrix (tim) measurement and x-ray fluoroscopy for intraoperative electrode array tip fold-over detection. *Otol Neurotol*, *42*, e1457–e1463.

Klein, S., Staring, M., Murphy, K., Viergever, M. A., Pluim, J. P. (2009). Elastix: A toolbox for intensity-based medical image registration. *IEEE Trans Med Imaging*, *29*, 196–205.

Kurz, A., Müller-Graff, F. -T., Hagen, R., Rak, K. (2022). One click is not enough: Anatomy-based fitting in experienced cochlear implant users. *Otol Neurotol*, *43*, 1176–1180.

Lambriks, L., van Hoof, M., Debruyne, J., Janssen, M., Hof, J., Hellingman, K., Devocht, E., George, E. (2023). Toward neural health measurements for cochlear implantation: The relationship among electrode positioning, the electrically evoked action potential, impedances and behavioral stimulation levels. *Front Neurol*, *14, 1093265*.

Leblans, M., Sismono, F., Vanpoucke, F., van Dinther, J., Lerut, B., Kuhweide, R., Offeciers, E., Zarowski, A. (2022). Novel impedance measures as biomarker for intracochlear fibrosis. *Hear Res, 426, 108563*.

Lee, J., Nadol Jr, J. B., Eddington, D. K. (2011). Factors associated with incomplete insertion of electrodes in cochlear implant surgery: A histo-pathologic study. *Audiol Neurootol*, *16*, 69–81.

Li, L., Wei, J., Chen, J. K., Wu, D., & Coelho, D. H. (2022). Early elevation and normalization of electrode impedance in patients with enlarged vestibular aqueduct undergoing cochlear implantation. *Otol Neurotol, 43*, e535−e539.

McCollough, C. H., Bushberg, J. T., Fletcher, J. G., Eckel, L. J. (2015). Answers to common questions about the use and safety of ct scans. *Mayo Clin Proc*, *90*, 1380–1392.

McNeill, C., & Eykamp, K. (2016). Cochlear implant impedance fluctuation in meniere's disease: A case study. *Otol Neurotol*, *37*, 873–877.

Mertens, G., Van de Heyning, P., Vanderveken, O., Topsakal, V., Van Rompaey, V. (2022). The smaller the frequency-to-place mismatch the better the hearing outcomes in cochlear implant recipients? *Eur Arch Otorhinolaryngol*, *279*, 1875–1883.

Minor, L. B., Schessel, D. A., & Carey, J. P. (2004). Meniere's disease. *Curr Opin Neurol*, *17*, 9–16.

Molisz, A., Zarowski, A., Vermeiren, A., Theunen, T., De Coninck, L., Siebert, J., Offeciers, E. F. (2015). Postimplantation changes of electrophysiological parameters in patients with cochlear implants. *Audiol Neurootol*, *20*, 222–228.

O'Connell, B. P., Cakir, A., Hunter, J. B., Francis, D. O., Noble, J. H., Labadie, R. F., Zuniga, G., Dawant, B. M., Rivas, A., & Wanna, G. B. (2016). Electrode location and angular insertion depth are predictors of audiologic outcomes in cochlear implantation. *Otol Neurotol*, *37*, 1016.

O'Connell, B. P., Holder, J. T., Dwyer, R. T., Gifford, R. H., Noble, J. H., Bennett, M. L., Rivas, A., Wanna, G. B., Haynes, D. S., Labadie, R. F. (2017). Intra-and postoperative electrocochleography may be predictive of final electrode position and postoperative hearing preservation. *Front Neurosci*, *11*, 291.

Parreño, M., Di Lella, F. A., Fernandez, F., Boccio, C. M., Ausili, S. A. (2020). Toward self-measures in cochlear implants: Daily and "home-made" impedance assessment. *Front Digit Health*, *2*, 33.

Pile, J., Sweeney, A. D., Kumar, S., Simaan, N., Wanna, G. B. (2017). Detection of modiolar proximity through bipolar impedance measurements. *Laryngoscope*, *127*, 1413–1419.

Rahman, M. T., Chari, D., Ishiyama, G., Lopez, I., Quesnel, A. M., Ishiyama, A., Nadol, J. B., Hansen, M. R. (2022). Cochlear implants: Causes, effects and mitigation strategies for the foreign body response and inflammation. *Hear Res, 422, 108536*.

Rathgeb, C., Demattè, M., Yacoub, A., Anschuetz, L., Wagner, F., Mantokoudis, G., Caversaccio, M., Wimmer, W. (2019). Clinical applicability of a preoperative angular insertion depth prediction method for cochlear implantation. *Otol Neurotol*, *40*, 1011–1017.

de Rijk, S. R., Tam, Y. C., Carlyon, R. P., Bance, M. L. (2020). Detection of extracochlear electrodes in cochlear implants with electric field imaging/transimpedance measurements:: A human cadaver study. *Ear Hear*, *41*, 1196–1207.

RStudio Team. (2022). *Rstudio: Integrated development environment for r*. RStudio, PBC. Boston, MA. http://www.rstudio.com/

Seyyedi, M., & Nadol J. B.Jr (2014). Intracochlear inflammatory response to cochlear implant electrodes in the human. *Otol Neurotol*, *35*, 1545.

Shaul, C., Bester, C. W., Weder, S., Choi, J., Eastwood, H., Padmavathi, K., Collins, A., O'Leary, S. J. (2019). Electrical impedance as a biomarker for inner ear pathology following lateral wall and perimodiolar cochlear implantation. *Otol Neurotol*, *40*, e518–e526.

Sijgers, L., Huber, A., Tabibi, S., Grosse, J., Roosli, C., Boyle, P., Koka, K., Dillier, N., Pfiffner, F., Dalbert, A. (2022). Predicting cochlear implant electrode placement using monopolar, three-point and four-point impedance measurements. *IEEE Trans Biomed Eng, 69*, 2533−2544.

Tykocinski, M., Cohen, L. T., Cowan, R. S. (2005). Measurement and analysis of access resistance and polarization impedance in cochlear implant recipients. *Otol Neurotol*, 26, 948–956.

Vanpoucke, F. J., Zarowski, A. J., Peeters, S. A. (2004). Identification of the impedance model of an implanted cochlear prosthesis from intra-cochlear potential measurements. *IEEE Trans Biomed Eng*, 51, 2174–2183.

Vargas, J. L., Sainz, M., Roldan, C., Alvarez, I., de la Torre, A. (2012). Long-term evolution of the electrical stimulation levels for cochlear implant patients. *Clin Exp Otorhinolaryngol*, 5, 194–200.

Venail, F., Mathiolon, C., De Champfleur, S. M., Piron, J. P., Sicard, M., Villemus, F., Vessigaud, M. A., Sterkers-Artieres, F., Mondain, M., Uziel, A. (2015). Effects of electrode array length on frequency-place mismatch and speech perception with cochlear implants. *Audiol Neurootol*, 20, 102–111.

Verbist, B. M., Skinner, M. W., Cohen, L. T., Leake, P. A., James, C., Boëx, C., Holden, T. A., Finley, C. C., Roland, P. S., RolandJr, J. T., Haller, M., Patrick, J. F., Jolly, C. N., Faltys, M. A., Briaire, J. J., Frijns, J. H. M. (2010). Consensus panel on a cochlear coordinate system applicable in histological, physiological and radiological studies of the human cochlea. *Otol Neurotol*, 31, 722.

Wimmer, W., Venail, F., Williamson, T., Akkari, M., Gerber, N., Weber, S., Caversaccio, M., Uziel, A., Bell, B. (2014). Semiautomatic cochleostomy target and insertion trajectory planning for minimally invasive cochlear implantation. *Biomed Res Int*, 2014, 1–8.

Wimmer, W., Vandersteen, C., Guevara, N., Caversaccio, M., Delingette, H. (2019). Robust cochlear modiolar axis detection in ct. *Med Image Comput Comput Assist Interv, 11768,* 3–10.

Wimmer, W., Sclabas, L., Caversaccio, M. D., Weder, S. (2022a). Cochlear implant electrode impedance as potential biomarker for residual hearing. *Front Neurol*, 13, 1305.

Wimmer, W., Soldati, F. O., Weder, S., Vischer, M., Mantokoudis, G., Caversaccio, M., Anschuetz, L. (2022b). Cochlear base length as predictor for angular insertion depth in incomplete partition type 2 malformations. *Int J Pediatr Otorhinolaryngol*, 159, 111204.

Wolf-Magele, A., Schnabl, J., Edlinger, S., Pok, S., Schoerg, P., Sprinzl, G. (2015). Postoperative changes in telemetry measurements after cochlear implantation and its impact on early activation. *Clin Otolaryngol*, 40, 527–534.

Xu, J., Xu, S. -A., Cohen, L. T., Clark, G. M. (2000). Cochlear view: Postoperative radiography for cochlear implantation. *Am J Otol*, 21, 49–56.

Zeng, F. -G. (2022). Celebrating the one millionth cochlear implant. *JASA Express Lett*, 2, 077201.

Zierhofer, C., Hochmair, I., Hochmair, E. (1997). The advanced combi 40+ cochlear implant. *Am J Otol*, 18, S37–S38.